Modulation of hydroxyl variability by ENSO in the absence of external forcing

Alexander J. Turner[a,b,1], Inez Fung[a], Vaishali Naik[c], Larry W. Horowitz[c], and Ronald C. Cohen[a,b]

[a]Department of Earth and Planetary Sciences, University of California, Berkeley, CA 94720; [b]College of Chemistry, University of California, Berkeley, CA 94720; and [c]Geophysical Fluid Dynamics Laboratory, National Oceanic and Atmospheric Administration (NOAA), Princeton, NJ 08540

Edited by Mark H. Thiemens, University of California at San Diego, La Jolla, CA, and approved July 27, 2018 (received for review May 1, 2018)

The hydroxyl radical (OH) is the primary oxidant in the troposphere, and the impact of its fluctuations on the methane budget has been disputed in recent years, however measurements of OH are insufficient to characterize global interannual fluctuations relevant for methane. Here, we use a 6,000-y control simulation of preindustrial conditions with a chemistry-climate model to quantify the natural variability in OH and internal feedbacks governing that variability. We find that, even in the absence of external forcing, maximum OH changes are 3.8 ± 0.8% over a decade, which is large in the context of the recent methane growth from 2007–2017. We show that the OH variability is not a white-noise process. A wavelet analysis indicates that OH variability exhibits significant feedbacks with the same periodicity as the El Niño–Southern Oscillation (ENSO). We find intrinsically generated modulation of the OH variability, suggesting that OH may show periods of rapid or no change in future decades that are solely due to the internal climate dynamics (as opposed to external forcings). An empirical orthogonal function analysis further indicates that ENSO is the dominant mode of OH variability, with the modulation of OH occurring primarily through lightning NO_x. La Niña is associated with an increase in convection in the Tropical Pacific, which increases the simulated occurrence of lightning and allows for more OH production. Understanding this link between OH and ENSO may improve the predictability of the oxidative capacity of the troposphere and assist in elucidating the causes of current and historical trends in methane.

hydroxyl | ENSO | La Niña | methane | tropospheric oxidative capacity

The hydroxyl radical (OH) is the primary oxidant for many non-CO_2 greenhouse gases (GHGs), such as methane, as well as a number of ozone-depleting substances (1, 2). As such, the burden and distribution of OH dictates the lifetime of many important atmospheric trace gases and will affect the global warming potential of many GHGs. However, we currently lack a predictive understanding of OH variability on decadal-to-centennial timescales, evidenced by the disagreement between global models in their simulation of OH trends (e.g., ref. 3). For example, Naik et al. (3) found large intermodel diversity in both the sign and magnitude of preindustrial to present-day OH changes, ranging from −12% to +14%.

Efforts to characterize the factors that control global mean OH have generally focused on the ozone photolysis frequency (J_{O_3}), specific humidity (q), sources of reactive nitrogen (S_N; i.e., NO_x), and sources of reactive carbon (S_C; e.g., methane, CO, and NMVOCs) (e.g., refs. 5–7). Specifically, Murray et al. (7) compared simulations of preindustrial and present-day conditions to derive the following relationship:

$$[\mathrm{OH}] \propto J_{O_3}\, q \frac{S_N}{S_C^{3/2}}. \quad [1]$$

The dependence on J_{O_3} and q is because production of OH on global scales is due to the photolysis of ozone in the presence of water vapor, dependence on S_N is because increases in NO_x result in faster recycling of OH via reaction of HO_2 or RO_2 with NO, and OH is inversely related with S_C because the dominant loss process for OH involves reactions with CO, methane, and NMVOCs. This relationship from Murray et al. (7) highlights the major factors that could drive changes in global mean OH.

Previous work from Turner et al. (8) and Rigby et al. (9) has shown how relatively small variations in OH (on the order of ∼3% over a 10-y period) can explain present trends in atmospheric methane; however, direct measurements of OH are neither sufficiently precise nor spatially dense enough to characterize global OH variations of this magnitude. Instead, previous work has used measurements of methyl chloroform (CH_3CCl_3) to indirectly estimate the global OH burden, since OH is the primary oxidant for methyl chloroform and the oxidation is slow enough to represent a global integral (e.g., refs. 10–13). Many of these previous studies have found OH to be well buffered (e.g., refs. 13–15). This has led to a number of recent studies assuming that OH is time-invariant (i.e., no interannual variability) when analyzing methane trends (e.g., refs. 16 and 17).

Previous work has identified the importance of the El Niño–Southern Oscillation (ENSO) in tropospheric ozone (e.g., refs. 18–20); however, there has been little work discussing the relationship between ENSO and OH. A notable exception is the work of Prinn et al. (10, 11), who discuss how ENSO may have impacted their methyl chloroform measurements at Samoa due to its location in the Western Pacific. They suggest a tentative link between warm, cloudy El Niño events and low OH. Krol and Lelieveld (21) also mention the impact of biomass burning on OH during El Niño. Here we use a coupled chemistry-climate

Significance

The hydroxyl radical (OH) is central to tropospheric chemistry, but current measurements are insufficient to assess its effects on year-to-year changes in atmospheric methane. We use a 6,000-y control simulation in a global coupled chemistry-climate model to study the natural variability of OH. We find that natural OH variability can produce (unforced) methane trends as large as the observed changes in methane over the last few decades. Additionally, we find a link between OH and La Niña. While we cannot directly measure annual global mean OH, we can use what we know about La Niña to improve our understanding of OH. This may, in turn, improve our understanding of recent methane trends.

Author contributions: A.J.T. designed research; A.J.T. performed research; V.N. and L.W.H. developed and ran the model; A.J.T., I.F., and R.C.C. analyzed data; A.J.T. wrote the paper; and I.F., V.N., L.W.H., and R.C.C. provided comments on the paper.

The authors declare no conflict of interest.

This article is a PNAS Direct Submission.

[1]To whom correspondence should be addressed. Email: alexjturner@berkeley.edu.

This article contains supporting information online at www.pnas.org/lookup/suppl/doi:10.1073/pnas.1807532115/-/DCSupplemental.

model to demonstrate how ENSO can induce OH variability and trends that are large enough to explain present trends in atmospheric methane even in the absence of changes in methane emissions.

Methods and Results

We use a 6,000-y preindustrial control simulation conducted with the Geophysical Fluid Dynamics Laboratory CM3 (GFDL-CM3) model. GFDL-CM3 incorporates an atmospheric chemistry model within the framework of the atmosphere, ocean, land, and sea-ice components (3, 22–24). Most pertinent to our application is the fully coupled tropospheric and stratospheric chemistry. The merged chemical scheme includes tropospheric chemistry based on MOZART-2 (Model for OZone and Related chemical Tracers; ref. 25; simulates atmospheric concentrations of 97 chemical species including aerosols) and stratospheric chemistry based on AMTRAC (Atmospheric Model with Transport and Chemistry; ref. 26). The isoprene mechanism in GFDL-CM3 does not include OH recycling pathways discussed in Taraborrelli et al. (27), and modifying the chemistry scheme to include the OH recycling mechanisms from isoprene oxidation could alter the OH variability in the model. GFDL-CM3 uses a cubed sphere grid with 48 × 48 cells per face, resulting in a native horizontal resolution ranging from ∼163 km to

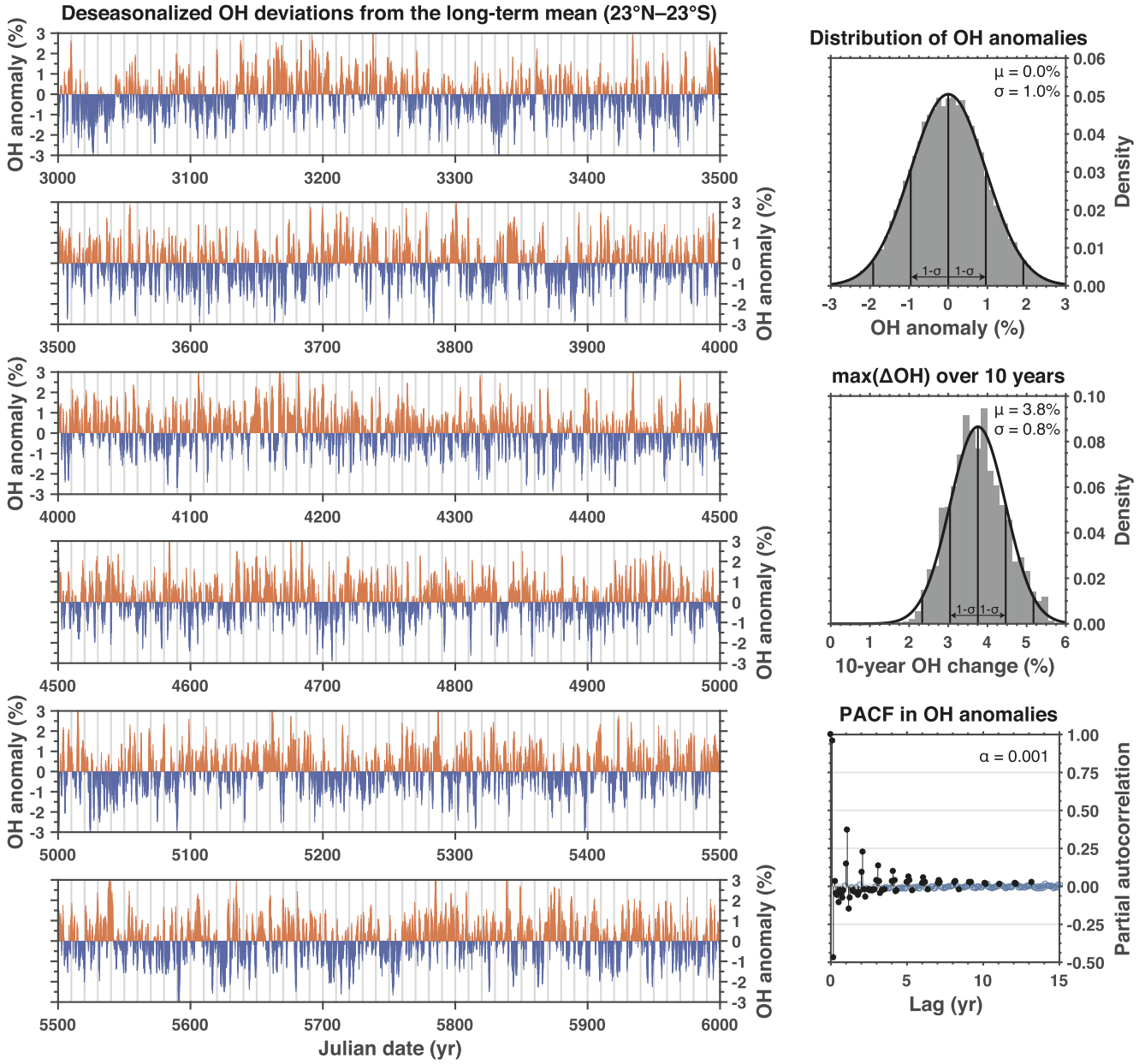

Fig. 1. Statistics of OH anomalies in a preindustrial control simulation. *Left* shows the monthly OH anomalies in the tropics (23°N–23°S) from years 3,000 to 6,000 in the GFDL-CM3 control run. OH anomalies are the deseasonalized OH deviations (pressure-weighted mean, 300 to 800 hPa) from the long-term mean, normalized to the long-term mean, and expressed as a percentage: $(x - \bar{x}) \cdot \bar{x}^{-1}$. Seasonal cycle is removed using a stable seasonal filter. *Top Right* shows the distribution of OH anomalies (gray bars) and a normal distribution fitted to the anomalies (black line). *Middle Right* is the maximum change in OH over a 10-y period (gray bars) and a normal distribution fitted to ΔOH (black line). *Bottom Right* is the partial autocorrelation function (PACF) of the OH anomalies; filled black circles indicate significant lags ($\alpha = 0.001$).

~231 km with 48 vertical layers. Results analyzed here are at monthly time resolution regridded to a horizontal resolution of $2^\circ \times 2.5^\circ$. This control simulation holds all forcings constant and uses prescribed (static) vegetation. Specifically, the land use and land cover, tropospheric ozone precursor emissions, solar and volcanic forcings, and GHG concentrations (including methane) are held at 1860 conditions. Production of NO_x by lightning is parameterized as a function of convective cloud-top height and thus varies with the model meteorology. Changes in stratospheric ozone concentrations can impact the photolysis in the troposphere. GFDL-CM3 has been shown to have a reasonable simulation of ENSO based on CMIP5 intercomparisons (28–34). The ENSO period is slightly short (~2.5 y), and its anomaly patterns and teleconnections tend to be shifted slightly west of observed [see figure 18 in Donner et al. (22)].

Fig. 1 shows the time series of the deseasonalized OH anomalies in the tropics (23°N–23°S) from years 3,000 to 6,000 in the control simulation. We use pressure-weighted tropospheric mean quantities from 300 to 800 hPa. [Boundary layer is excluded because concentrations of methane are prescribed below 800 hPa, which may dampen the potential variability and feedbacks. Using the full tropospheric column makes little difference in the periodicity (see *SI Appendix*, Fig. S1).] The first 3,000 y of the control simulation are discarded due to a climate drift of $\sim 1^\circ$C temperature increase and a change in computer architecture in year 1,070 of the control simulation that resulted in a ~4% increase in global mean OH (see *SI Appendix*, Fig. S2). From Fig. 1, we find an OH interannual variability of $\pm 1.0\%$ (1-σ). This variability is consistent with previous work that finds global mean OH to be well buffered [e.g., Montzka et al. (13), who infer an interannual variability of $2.3 \pm 1.5\%$ using observations of methyl chloroform]. However, the present atmosphere is substantially NO_x-richer than the preindustrial, and we may expect more OH recycling in the present. A qualitative examination of the OH anomaly time series shows regular excursions to $\pm 2\%$ for individual decades. These excursions could lead to transients in the atmospheric record for molecules whose atmospheric lifetime is dictated by OH, such as methane. To determine the distribution of decadal-scale changes in OH, we randomly draw decades from this 3,000-y control simulation and compute the maximum change in OH over a decade (ΔOH). We find ΔOH over a decade is $3.8 \pm 0.8\%$ (see Fig. 1, *Middle Right*). These changes in OH alone are large enough to explain present trends in methane, independent of changes in methane sources.

The distribution of decadal changes in OH provides evidence of atmospherically relevant changes in OH in the absence of external forcing. However, it does not indicate whether this simply arises from random sampling of a white-noise process or if there is a mechanism that could provide longer term feedbacks. To investigate the possibility of feedbacks, we compute the partial autocorrelation function (PACF) of the OH anomalies. Black dots in Fig. 1, *Bottom Right* indicate lags that are significant at the 99.9% level ($\alpha = 0.001$). We find numerous significant, large lags between 0 and 5 y as well as significant, but weaker, lags going out 10+ y. This indicates that there are feedbacks in

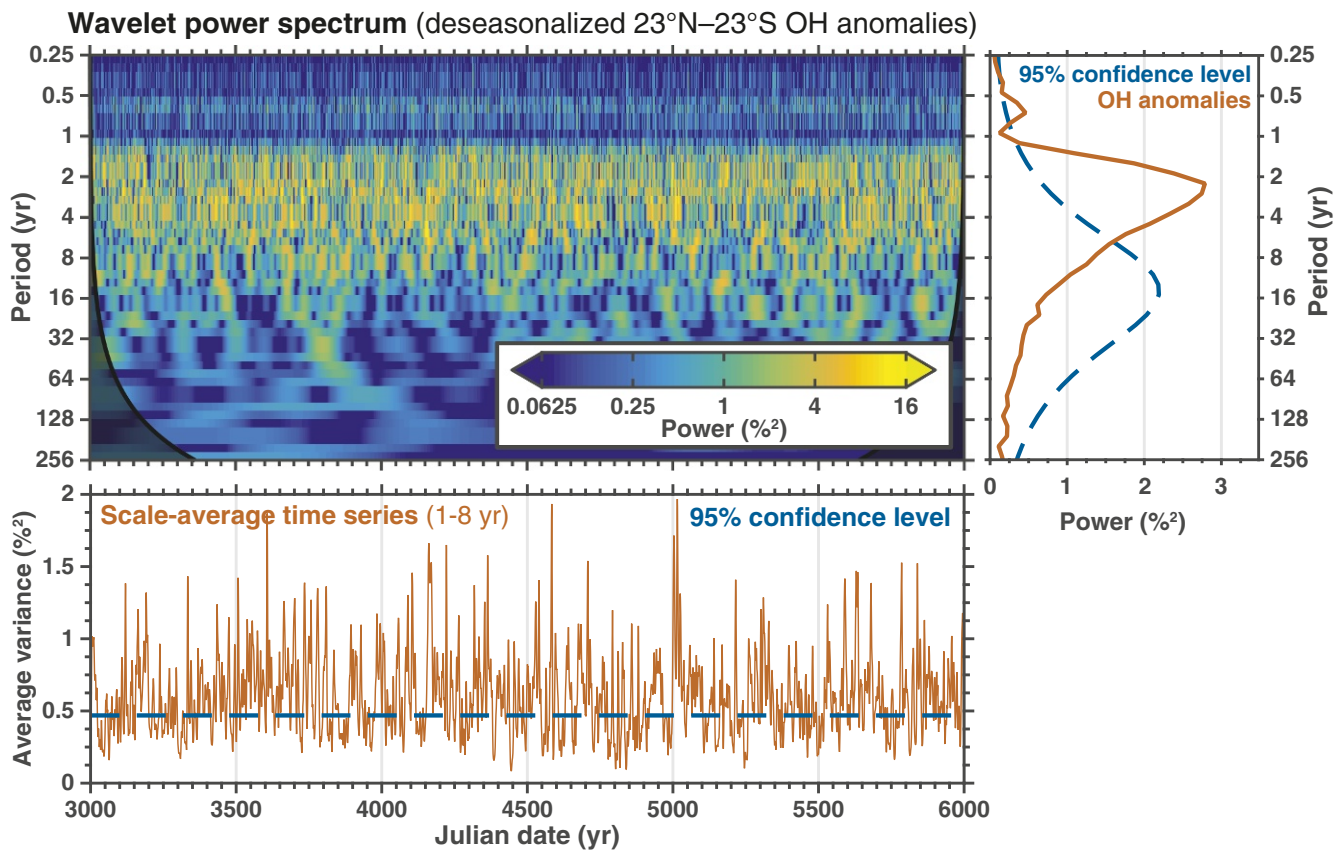

Fig. 2. Wavelet analysis of the OH anomalies (300 to 800 hPa) in a preindustrial control simulation. *Top Left* is the bias-rectified local wavelet power spectrum of the OH anomalies from Fig. 1 using a Morlet wavelet following Torrence and Compo (4). Left axis is the Fourier period (in years), bottom axis is time (in years), and shading is the power (in $\%^2$). *Right* is the global wavelet spectrum for the OH anomalies (solid red line) and the 95% confidence level (dashed blue line) assuming red noise. *Bottom* is the scale-averaged wavelet power over the 1–8 y band for the OH anomalies (solid red line) and the 95% confidence level (dashed blue line) assuming red noise.

the chemistry or climate system that are providing some memory in the OH anomalies.

Since OH variability exhibits significant feedbacks on annual-to-decadal timescales, we examine the question: "What is the mechanism providing this memory in OH?" Fig. 2 shows the wavelet power spectrum for the deseasonalized OH anomalies from years 3,000 to 6,000 in the GFDL-CM3 control simulation using a Morlet wavelet following Torrence and Compo (4). We see a strong periodicity in the OH anomalies that peaks at ∼3 y (Fig. 2, *Right*). The power spectrum found here bears a strong resemblance to that of ENSO, diagnosed from the NINO3.4 SST anomalies (see *SI Appendix*, Fig. S3). Fig. 2, *Bottom* shows how the variance changes over time when averaged over 1- to 8-y periods. We find modulation of the OH variability that is entirely due to the internal climate dynamics—that is to say, that it is intrinsically generated variability and not driven by a change in forcings.

This modulation of the OH variability in the absence of external forcing is striking. We find periods of large variability (e.g., years 5,000 to 5,050) and quiescent periods (years 4,800 to 4,850). If the real-world OH is similarly modulated, then it is possible that the research community could have observed an unrepresentative ∼15 y of OH variability in the recent record, confounding attempts to attribute observed methane trends to forced changes in sources or sinks. This finding of modulation in the OH variability also has implications for future methane trends. It implies that the envelope of potential methane trajectories may be larger than previously assumed due to this nonstationary variability in the sink. In other words, we could observe transients in the methane record that arise from variability in OH, independent of changes in methane sources. This would be superimposed onto the trends due to external forcings (e.g., methane emissions).

Analysis shown in Fig. 2 indicates the OH anomalies have a periodicity similar to ENSO. We further investigate the link to ENSO by examining the spatial patterns of OH. Fig. 3*A* shows the climatology of OH with a peak OH concentration off the coast of Africa. However, much of this spatial pattern is dictated by the seasonal cycle. Fig. 3*B* shows the spatial variability in OH that is not associated with the seasonal cycle. We find some of the largest variability in the Tropical Pacific, Eastern Africa, and the Indo-Gangetic Plain. This is surprising because the Tropical Pacific, with little OH (e.g., ref. 35), is not a region that would stand out as important from a qualitative examination of the OH climatology in Fig. 3*A*.

We compute the EOFs and the associated principal components (PCs) to identify the spatial patterns that explain the most variability in the OH anomalies. Fig. 3*C* shows the first EOF, which explains 17% of the variance in the OH anomalies. The second EOF (*SI Appendix*, Fig. S4) explains 7% of the variance. The leading EOF is found to be robust, but it is unclear if the second EOF is a robust pattern, and EOFs 3+ are not robust (*SI Appendix*, Fig. S5). We also find that EOF 1 explains 25 ± 3% of the variance if we focus on 100-y records (*SI Appendix*, Fig. S6), indicating that this pattern of variability may be more important on decadal-to-centennial timescales. The EOF 1 pattern and PC 1 time series are strongly indicative of ENSO. Specifically, from Fig. 3*C* we see that EOF 1 has a dipole feature in the Tropical Pacific and PC 1 is anticorrelated with the NINO3.4 SST anomalies ($r = -0.84$; Fig. 3*D*). From this we conclude that ENSO is the dominant factor controlling the OH variability in the absence of external forcings.

There are a number of mechanisms through which ENSO could impact OH. ENSO could affect (*i*) J_{O_3} by changing the Walker circulation and stratospheric ozone, (*ii*) q through changes in temperature via Clausius–Clapeyron, (*iii*) S_N through changes to convection and consequently emissions of NO_x from lightning, and (*iv*) S_C through changes to biomass burning or wetland or biogenic VOC emissions. The fourth mechanism is not feasible here because GHG concentrations are prescribed and biomass burning and biogenic VOC emissions are unchanging in the preindustrial control simulation. We find the strongest correlation between OH and lightning NO_x emission anomalies ($r = 0.52$; see *SI Appendix*, Fig. S7), indicating that changes in NO_x emissions from lightning are the primary mechanism through which ENSO is modulating OH. This is reinforced by a strong correlation between the lightning NO_x emission anomalies and the leading PC ($r = 0.78$; see *SI Appendix*, Fig. S8).

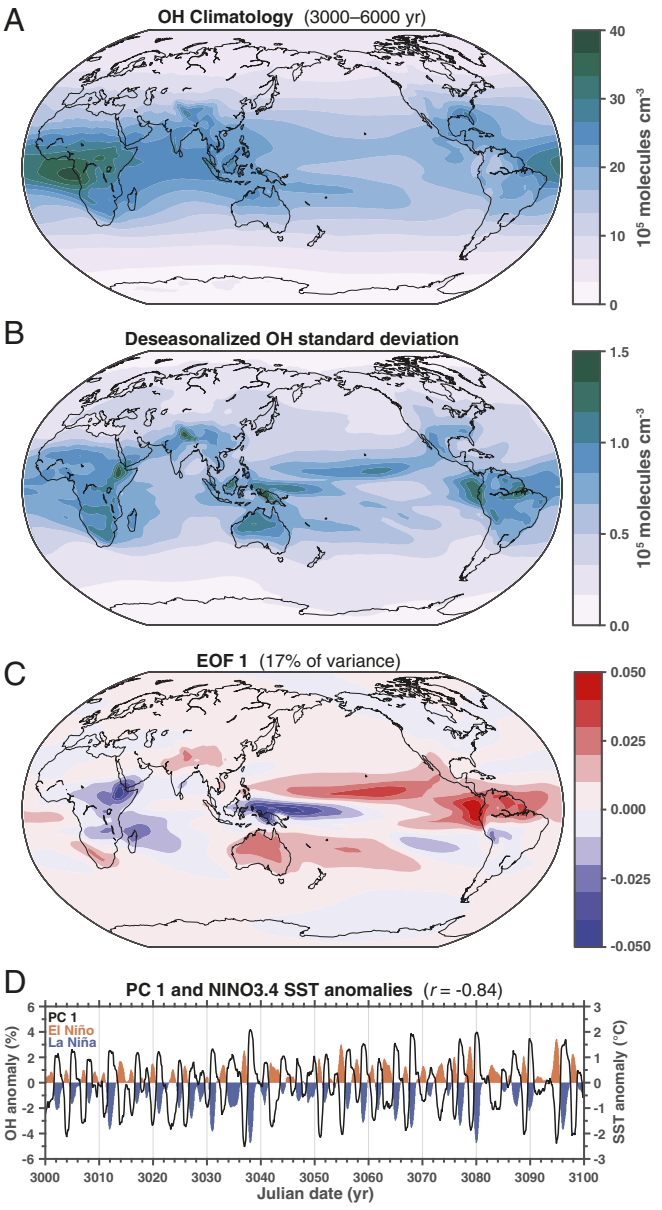

Fig. 3. Modes controlling the OH variability in a preindustrial control simulation. *A* shows the OH climatology (300 to 800 hPa) from years 3,000 to 6,000. *B* shows the deseasonalized OH standard deviation where each grid cell is deseasonalized using a unique stable seasonal filter. *C* shows the first empirical orthogonal function (EOF) that explains 17% of the variance in the OH anomalies. EOF is unit length (sum of the squares is equal to 1) and computed using the spatially weighted [$\sqrt{\cos(lat)}$], unnormalized OH deviations ($x - \bar{x}$). *D* shows the first PC (black line) that corresponds to the first EOF. Only the first 100 y (out of 3,000 y) is shown for the PC. Red and blue shading in *D* are the NINO3.4 SST anomalies (area-averaged sea surface temperature anomalies from 5°S–5°N and 170°W–120°W).

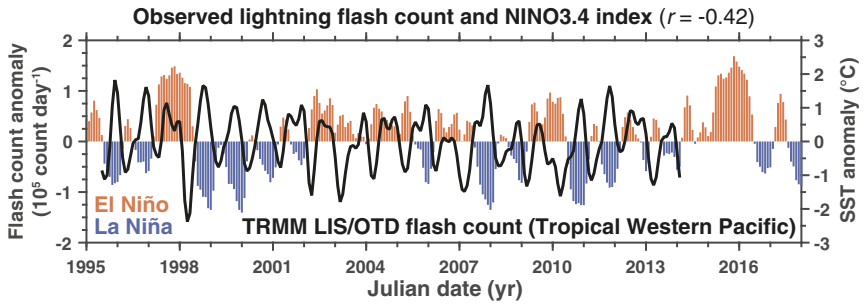

Fig. 4. Lightning flash counts and ENSO in the present-day. Shown are lightning flash count anomalies seen by the Lightning Imaging Sensor (LIS) and Optical Transient Detector (OTD) on the Tropical Rainfall Measuring Mission (TRMM) satellite (solid black line; https://lightning.nsstc.nasa.gov/data/data_lis-otd-climatology.html) in the Tropical Western Pacific (23°N–23°S; 125°E–85°W) and the NINO3.4 SST index (red and blue shading) from the Extended Reconstructed Sea Surface Temperature v5 (ERSSTv5; https://www.esrl.noaa.gov/psd/data/climateindices/list/). *SI Appendix*, Fig. S9 shows the SSTs in the Tropical Pacific from 1980–2017.

This is not to say that changes in q or J_{O_3} are unimportant; it means that S_N is the largest lever on OH in the GFDL-CM3 model and highlights the importance of understanding how tropical lightning may change in the future (e.g., ref. 36). There will also be other indirect effects from changes in S_N [e.g., Murray et al. (7) discuss how changing NO_x could influence ozone production and thus the primary source of HO_x]. Mechanistically, this means that in this model periods of La Niña lead to increased deep convection in the Tropical Pacific that increases the NO_x produced from lightning and, consequently, increases the recycling of OH. We find tenuous evidence of this relationship between La Niña and Tropical Pacific lightning flash counts in the present-day satellite record (Fig. 4), in agreement with previous work that found a relationship between maritime lightning and La Niña (e.g., ref. 37).

Conclusions

A 6,000-y preindustrial control simulation of the GFDL-CM3 model shows OH variability that is large enough to impact our understanding of present and future trends in atmospheric methane. We also find strong modulation of the OH variability, intrinsically generated by the model, in the absence of external forcings. The finding of intrinsically generated modulation of OH variability bares resemblance to work on ENSO from Wittenberg (38), who showed strong interdecadal and intercentennial modulation of ENSO in a preindustrial control simulation. A wavelet and EOF analysis of the OH anomalies indicate that ENSO is the dominant factor controlling this OH variability. Periods of La Niña are found to be positively correlated with increases in OH. This is primarily due to increases in the occurrence of lightning in the Tropical Pacific during La Niña, which in turn lead to more recycling of OH. This relationship between lightning in the Tropical Pacific and La Niña is also seen in the present-day record of lightning and ENSO, lending credence to this link.

This link between ENSO and OH may help improve the predictability of the oxidative capacity of the troposphere. While we cannot directly measure OH to a precision that is necessary to understand present trends in some non-CO_2 GHGs, we may be able to use information about ENSO to reduce our uncertainty on OH. Such a relationship can help improve the predictability of OH and, consequently, methane. Moving forward, this relationship could be used as a weak constraint when estimating OH or methane through inverse methods.

ACKNOWLEDGMENTS. We thank C. Frankenberg, J. C. H. Chiang, and A. T. Wittenberg for helpful comments on the work. A.J.T. is supported as a Miller Fellow with the Miller Institute for Basic Research in Science at University of California, Berkeley. R.C.C. acknowledges support from NASA Grant NNX15AE37G. This research used the Savio computational cluster resource provided by the Berkeley Research Computing program at the University of California, Berkeley (supported by the University of California, Berkeley Chancellor, Vice Chancellor for Research, and Chief Information Officer). This research also used resources from the National Energy Research Scientific Computing Center, which is supported by the Office of Science of the US Department of Energy under Contract DE-AC02-05CH11231.

1. Prather MJ, Holmes CD, Hsu J (2012) Reactive greenhouse gas scenarios: Systematic exploration of uncertainties and the role of atmospheric chemistry. *Geophys Res Lett* 39:L09803.
2. IPCC (2013) Climate change 2013: The physical science basis. Contribution of working group i to the fifth assessment report of the Intergovernmental Panel on Climate Change (IPCC) (Cambridge Univ Press, New York), technical report.
3. Naik V, et al. (2013) Preindustrial to present-day changes in tropospheric hydroxyl radical and methane lifetime from the Atmospheric Chemistry and Climate Model Intercomparison Project (ACCMIP). *Atmos Chem Phys* 13:5277–5298.
4. Torrence C, Compo GP (1998) A practical guide to wavelet analysis. *Bull Am Meteorol Soc* 79:61–78.
5. Wang Y, Jacob DJ (1998) Anthropogenic forcing on tropospheric ozone and OH since preindustrial times. *J Geophys Res Atmospheres* 103:31123–31135.
6. Holmes CD, Prather MJ, Svde OA, Myhre G (2013) Future methane, hydroxyl, and their uncertainties: Key climate and emission parameters for future predictions. *Atmos Chem Phys* 13:285–302.
7. Murray LT, et al. (2014) Factors controlling variability in the oxidative capacity of the troposphere since the last glacial maximum. *Atmos Chem Phys* 14:3589–3622.
8. Turner AJ, Frankenberg C, Wennberg PO, Jacob DJ (2017) Ambiguity in the causes for decadal trends in atmospheric methane and hydroxyl. *Proc Natl Acad Sci USA* 114:5367–5372.
9. Rigby M, et al. (2017) Role of atmospheric oxidation in recent methane growth. *Proc Natl Acad Sci USA* 114:5373–5377.
10. Prinn RG, et al. (2001) Evidence for substantial variations of atmospheric hydroxyl radicals in the past two decades. *Science* 292:1882–1888.
11. Prinn RG, et al. (2005) Evidence for variability of atmospheric hydroxyl radicals over the past quarter century. *Geophys Res Lett* 32:L07809.
12. Prinn RG (2003) The cleansing capacity of the atmosphere. *Annu Rev Environ Resour* 28:29–57.
13. Montzka SA, et al. (2011) Small interannual variability of global atmospheric hydroxyl. *Science* 331:67–69.
14. Lelieveld J, Dentener FJ, Peters W, Krol MC (2004) On the role of hydroxyl radicals in the self-cleansing capacity of the troposphere. *Atmos Chem Phys* 4:2337–2344.
15. Lelieveld J, Gromov S, Pozzer A, Taraborrelli D (2016) Global tropospheric hydroxyl distribution, budget and reactivity. *Atmos Chem Phys* 16:12477–12493.
16. Schaefer H, et al. (2016) A 21st-century shift from fossil-fuel to biogenic methane emissions indicated by $^{13}ch_4$. *Science* 352:80–84.
17. Schwietzke S, et al. (2016) Upward revision of global fossil fuel methane emissions based on isotope database. *Nature* 538:88–91.
18. Ziemke JR, Chandra S (2003) La Nina and El Nino–induced variabilities of ozone in the tropical lower atmosphere during 1970-2001. *Geophys Res Lett* 30:1142.
19. Doherty RM, Stevenson DS, Johnson CE, Collins WJ, Sanderson MG (2006) Tropospheric ozone and El Niño–Southern Oscillation: Influence of atmospheric dynamics, biomass burning emissions, and future climate change. *J Geophys Res* 111: D19304.
20. Oman LD, et al. (2011) The response of tropical tropospheric ozone to ENSO. *Geophys Res Lett* 38:L13706.
21. Krol M, Lelieveld J (2003) Can the variability in tropospheric oh be deduced from measurements of 1,1,1-trichloroethane (methyl chloroform)? *J Geophys Res Atmos* 108:4125.

22. Donner LJ, et al. (2011) The dynamical core, physical parameterizations, and basic simulation characteristics of the atmospheric component AM3 of the GFDL global coupled model CM3. *J Clim* 24:3484–3519.
23. Griffies SM, et al. (2011) The GFDL CM3 coupled climate model: Characteristics of the ocean and sea ice simulations. *J Clim* 24:3520–3544.
24. Shevliakova E, et al. (2009) Carbon cycling under 300 years of land use change: Importance of the secondary vegetation sink. *Glob Biogeochem Cycles* 23: GB2022.
25. Horowitz LW, et al. (2003) A global simulation of tropospheric ozone and related tracers: Description and evaluation of Mozart, version 2. *J Geophys Res Atmos* 108:4784.
26. Austin J, Wilson RJ (2006) Ensemble simulations of the decline and recovery of stratospheric ozone. *J Geophys Res* 111:D16314.
27. Taraborrelli D, et al. (2012) Hydroxyl radical buffered by isoprene oxidation over tropical forests. *Nat Geosci* 5:190–193.
28. Graham FS, Wittenberg AT, Brown JN, Marsland SJ, Holbrook NJ (2016) Understanding the double peaked El Niño in coupled GCMS. *Clim Dyn* 48:2045–2063.
29. Chen C, Cane MA, Wittenberg AT, Chen D (2017) Enso in the CMIP5 simulations: Life cycles, diversity, and responses to climate change. *J Clim* 30:775–801.
30. Bellenger H, Guilyardi E, Leloup J, Lengaigne M, Vialard J (2013) Enso representation in climate models: From CMIP3 to CMIP5. *Clim Dyn* 42:1999–2018.
31. Yun KS, Yeh SW, Ha KJ (2016) Inter-El Niño variability in CMIP5 models: Model deficiencies and future changes. *J Geophys ResAtmos* 121:3894–3906.
32. Ferrett S, Collins M, Ren HL (2017) Understanding bias in the evaporative damping of El Niño–Southern Oscillation events in CMIP5 models. *J Clim* 30:6351–6370.
33. Taschetto AS, et al. (2014) Cold tongue and warm pool ENSO events in CMIP5: Mean state and future projections. *J Clim* 27:2861–2885.
34. Grose MR, et al. (2014) Assessment of the CMIP5 global climate model simulations of the western tropical pacific climate system and comparison to CMIP3. *Int J Climatology* 34:3382–3399.
35. Rex M, et al. (2014) A tropical west pacific OH minimum and implications for stratospheric composition. *Atmos Chem Phys* 14:4827–4841.
36. Finney DL, et al. (2018) A projected decrease in lightning under climate change. *Nat Clim Change* 8:210–213.
37. Sátori G, Williams E, Lemperger I (2009) Variability of global lightning activity on the ENSO time scale. *Atmos Res* 91:500–507.
38. Wittenberg AT (2009) Are historical records sufficient to constrain ENSO simulations? *Geophys Res Lett* 36L12702.